Biomedical Signal Processing and Control 126 (2026) 110940

Contents lists available at ScienceDirect

Biomedical Signal Processing and Control

journal homepage: www.elsevier.com/locate/bspc

Efficient and robust fluorescence molecular tomography reconstruction via sparse pseudo-input Gaussian process based Bayesian optimization

Xin Cao [a], Yiting He [a], Xin Zhou [a], Jiaxin Du [a], Yi Chen [a,b,*], Chengyi Gao [c], Huangjian Yi [a], Xingxing Hao [a,*], Linzhi Su [a]

[a] College of Computer Science, Northwest University, Xi'an, Shaanxi 710127, China
[b] School of Electrical and Mechanical Engineering, The University of Adelaide, Adelaide, SA 5005, Australia
[c] Department of Oncology, The First Affiliated Hospital, Xi'an Jiaotong University, Xi'an, Shaanxi 710061, China

ARTICLE INFO

Keywords:
Fluorescence Molecular Tomography
Bayesian Optimization
Gaussian Processes
Sparse Reconstruction
Elastic-Net Regularization

ABSTRACT

Accurate reconstruction in Fluorescence Molecular Tomography (FMT) is challenging due to the severe scattering of light in tissues and the computational burden of solving the inverse problem. In this work, we propose a high-efficiency Bayesian optimization strategy, termed SCBO, which integrates Sparse Pseudo-input Gaussian Processes (SPGP) with Constrained Least Squares Fitting (CLSF). The core of SCBO lies in replacing the computationally expensive full Gaussian Process model with an SPGP that approximates the covariance structure via limited inducing points, reducing complexity from cubic to linear scales. To mitigate the ill-posedness, Elastic-Net regularization is incorporated to provide a tunable balance between L1-based sparsity and L2-based smoothing, ensuring enhanced structural fidelity. Furthermore, the optimization landscape is explored efficiently using a CLSF acquisition function approximated via Monte Carlo sampling. Experimental results from heterogeneous phantoms and *in vivo* biological models indicate that SCBO achieves superior localization accuracy (Position Error $\approx$ 0.3–0.4 mm) and morphological similarity (Dice coefficient $>$ 0.8) compared to graph-total variation and sparse Bayesian learning approaches, offering a robust solution for deep-tissue fluorescence reconstruction.

1. Introduction

Fluorescence molecular imaging (FMI) is a powerful non-invasive modality used to detect the surface fluorescence distribution emitted from biological tissues by employing high-sensitivity detectors, such as charge-coupled device (CCD) cameras, scientific complementary metal–oxide–semiconductor (sCMOS) cameras, photomultiplier tubes (PMTs), and other photosensitive instruments [1–3]. However, owing to the absorption and scattering of light during tissue propagation, only photon distribution information on the surface can be captured by FMI, while three-dimensional (3D) spatial information of the fluorescent target remains inaccessible [4]. To address this limitation, fluorescence molecular tomography (FMT) has been developed as an imaging modality based on FMI. In FMT, the correspondence between surface fluorescence measurements and internal fluorescent probe distributions is established, and reconstruction algorithms are applied to recover the spatial configuration of probes within tissues, thereby enhancing the resolution of deep-seated structures [5]. Nevertheless, due to the strong scattering properties of fluorescence in biological tissues, the FMT reconstruction problem is inherently ill-conditioned [6].

To improve the accuracy of FMT reconstruction, constraints are imposed during the inverse computation. In recent years, multiple regularization schemes have been introduced to confine the admissible solution domain [7], including the use of L_p-norm regularization ($p \in [0,2]$) to constrain FMT reconstruction. However, different values of p are suitable for distinct reconstruction scenarios. When the value of p is small, such as in L_0 and L_1 norms [8], it can accurately recover portions of true sources but frequently fails to preserve detailed boundary information. As a result, methods derived from L_1-norm regularization, including the primal–dual interior-point (PDIP) method, non-convex sparse regularization approach, and incomplete variable truncated conjugate gradient (IVTCG) method have been developed [9–11]. Conversely, when the value of p is large, such as in L_2 and L_p norms [8], they are more appropriate for morphological reconstruction. Nevertheless, higher p values often generate artifacts and over-smooth

* Corresponding authorsat: College of Computer Science, Northwest University, Xi'an, Shaanxi 710127, China.
E-mail addresses: yichen.cgz@gmail.com (Y. Chen), xingxing.hao@nwu.edu.cn (X. Hao).

https://doi.org/10.1016/j.bspc.2026.110940
Received 11 December 2025; Received in revised form 11 June 2026; Accepted 27 June 2026
Available online 30 June 2026

the reconstructed structures. To overcome these limitations, forward–backward splitting L_1-L_2 norm regularization and joint $L_{1/2}$-norm models with nonconvex Laplacian manifold regularization have been introduced [12,13]. Moreover, advanced regularization approaches based on L_p-norm, including elastic-net (EN) regularization, logarithmic total variation (Log-TV), and graph total variation (Graph-TV), have been proposed [14–16]. While these methods can yield satisfactory results, their performance is often highly dependent on the careful tuning of regularization parameters. Furthermore, they can be computationally intensive and may still offer limited fidelity in boundary delineation.

However, boundary information of biological tissues is particularly important in practical applications. Therefore, dictionary learning methods have been proposed. In these approaches, fluorescence signals are represented as linear combinations of dictionary elements constructed from redundant dictionaries, and prior knowledge is incorporated to enhance reconstruction accuracy [17]. Representative methods include look-ahead orthogonal matching pursuit (LAOMP), sparse gradient domain adaptive dictionary learning, and recursive least squares dictionary learning algorithm (RLS-DLA) [18–20]. Meanwhile, inspired by compressed sensing theory, collaborative dictionary learning method have been introduced [21] to further increase the diversity and complementarity among dictionaries. In addition, convolutional dictionary learning (CDL) has been developed to further improve algorithmic efficiency [22]. Although dictionary learning approaches can offer more detailed boundary information, they are often hampered by high computational complexity and slow convergence speeds.

In recent years, the rapid advancement of deep learning has introduced new methodologies for FMT reconstruction. By utilizing layer-by-layer feature extraction, deep learning overcomes the inherent limitations of traditional regularization methods and dictionary learning, demonstrating exceptional capabilities in addressing inverse problem [23]. To achieve ultra-high spatial resolution in FMT reconstruction, 3-D fusion dual-sampling deep neural network (UHR-DeepFMT) [24] and multi-scale deep residual network (MSDRN) [25] have been proposed. Moreover, in order to further enhance image quality, 3D deep encoder–decoder network (3D-En-Decoder), k-nearest neighbor based locally connected network (KNN-LC), and single-view reconstruction network (SVRNet) have been introduced [26–28]. While these deep learning-driven techniques are capable of significantly improving reconstruction accuracy, challenges related to interpretability persist, and the computational complexity remains high. The effectiveness of these methods in live samples still requires further validation.

As an alternative, Bayesian frameworks have garnered significant interest for their potential stability and efficiency. These methods integrate sparse priors with observed data, iteratively updating a posterior distribution via Bayes' theorem to estimate the unknown parameters [29]. Hierarchical Bayesian, naive Bayesian, and empirical Bayesian frameworks [30–32] have been introduced, substantially reducing computational demands. Subsequently, sparse Bayesian techniques were further advanced, resulting in sparse Bayesian learning based on Laplace distribution (SBL-LCGL) and adaptive grouping block sparse Bayesian learning (AGBSBL) [33,34], which improve both the accuracy and robustness of sparse representations and enhance reconstruction performance. In parallel, variational Bayesian methods [35] and Bayesian optimization approaches [36] have been extensively explored and refined. Notable developments include an adaptive online variational Bayesian method based on the normal-generalized inverse Gaussian prior (AOVB-NGIG) [37], dual-phase multiobjective Bayesian optimization method (DPMO-BO) [38], adaptive Bayesian augmented lagrangian algorithm (ABAL) [39], and Bayesian penalized likelihood reconstruction algorithm (BPL) [40]. However, these Bayesian methods exhibit sensitivity to the choice of prior distributions, which significantly restricts their broader applicability.

In this work, a Bayesian optimization method based on sparse pseudo-input Gaussian processes and constrained least squares fitting (SCBO) is proposed for FMT reconstruction. The central idea involves the generation of M inducing points to approximate the covariance matrix of the original N data points, thereby markedly reducing computational complexity. To further improve reconstruction quality while maintaining both the sparsity and morphology of the source distribution, elastic-net (EN) regularization is employed. EN regularization integrates L_1 and L_2 norms through weighting parameters, which balance sparsity and shape preservation, yielding an optimization problem equivalent to the original formulation and mitigating discontinuities in reconstructed tumor regions. During the optimization procedure, the acquisition function is constructed using the Monte Carlo (MC) method, and the constrained least squares fitting (CLSF) guides the sampling process to efficiently approach the optimal solution within a limited number of evaluations. Finally, the performance of the SCBO method is assessed through numerical simulations and implantation experiments. Comparative analyses with graph total variation (Graph-TV), recursive least squares dictionary learning algorithm (RLS-DLA), and sparse Bayesian learning based on Laplace distribution (SBL-LCGL) indicate that SCBO substantially enhances both the reconstruction accuracy and shape fidelity of fluorescent probe distributions relative to these methods.

The organization of this paper is as follows: Section 2 presents the FMT forward propagation and the SCBO method. Section 3 describes the experimental setup. Section 4 displays the experimental results. Section 5 offers a discussion and conclusion of our work.

2. Methodology

2.1. Forward propagation

In fluorescence molecular tomography (FMT), imaging relies on the propagation of near-infrared (NIR) light through biological tissue. This process is dominated by strong scattering and absorption, which complicates the modeling of photon transport. While the radiative transfer equation (RTE) [41] provides a highly accurate description of this process, its computational burden is prohibitive for most practical applications. Consequently, in highly scattering (diffusive) media such as tissue, the diffusion equation (DE) [42] is widely adopted as a computationally tractable and valid approximation.

For continuous-wave (CW) excitation, the propagation of excitation light and the subsequent emission of fluorescent light are governed by a set of coupled diffusion equations:

$$\begin{cases} \nabla \bullet [D_x(r)\nabla\Phi_x(r)] - \mu_{ax}(r)\Phi_x(r) = -\Theta\delta(r - r_s), r \in \Omega \\ \nabla \bullet [D_n(r)\nabla\Phi_n(r)] - \mu_{an}(r)\Phi_n(r) = -\eta\Phi_x(r)\mu_{af}(r), r \in \Omega \end{cases} \tag{1}$$

where ∇ is the gradient operator, and $D_{x,n} = 1/(3[\mu_{ax,an} + (1-g)\mu_{sx,sn}])$ is the diffusion coefficient. Here, g is the anisotropy factor. $D_x(r)$ and $D_n(r)$ are the diffusion coefficients of the excitation and emission light. $\Phi_x(r)$ and $\Phi_n(r)$ are the photon densities of the excitation and emission light at position r. μ_{ax} and μ_{an} are the absorption coefficients of the excitation and emission light. r is the position of the excitation source, whose excitation intensity is Θ, located beneath the surface Ω, with the unit defined as the mean free path of photon transport. $\delta(r)$ is the Dirac delta function, and η is the quantum yield, representing the efficiency of converting excitation light into fluorescence. $\mu_{af}(r)$ is the absorption coefficient of fluorescence for the excitation light, and Ω is the imaging domain.

Using the finite element method (FEM), the light propagation model is discretized, and the partial differential Eq. (1) is linearized into the following algebraic equation:

$$\begin{cases} M_x\Phi_x = S_x \\ M_n\Phi_n = G_xX \end{cases} \tag{2}$$

where M_x and M_n are the forward system matrices for the propagation of excitation and emission light. S_x is the vector representing the

distribution of discrete excitation point sources. G_x is defined as $G_x(i,j) = \int_\Omega \Phi_x(r)T_i(r)T_j(r)dr$, where $T_i(r)$ and $T_j(r)$ are the basis functions corresponding to nodes i and j.

Eq. (2) is further represented in a matrix form:

$$\Phi_n = {M_n}^{-1}GX = A_nX \tag{3}$$

where Φ_n is the data acquired from the body surface.

According to Eq. (3), a final linear mapping between the fluorescence yield within the imaging domain and the surface-measured data is established and is represented as:

$$\Phi = \mathrm{AX} \tag{4}$$

where Φ is the measurable fluorescence data on the specimen's surface, A is the system matrix, X is the unknown fluorescence yield distribution within the tissue that we seek to reconstruct. Therefore, within the aforementioned linear matrix equation, the fluorescence intensity distribution X is reconstructed and is essential for addressing the inverse problem in FMT.

In general, Eq. (4) cannot be directly solved for X due to its ill-conditioned nature. Therefore, elastic net (EN) regularization [43] is employed to balance the sparsity and smoothness of the reconstructed image, and the objective function is expressed as the sum of a least-squares term and a regularization component. It is defined as follows:

$$\min_X E(X) = \frac{1}{2}||AX - \Phi||_2^2 + \alpha(\beta||X||_1 + \frac{(1-\beta)}{2}||X||_2^2) \tag{5}$$

where $E(X)$ is the objective function to be minimized, α and β are the EN regularization parameters. Meanwhile, as the L_1-norm is non-differentiable at zero, the solver is enhanced through the SCBO method to mitigate non-smoothness challenges.

2.2. Reconstruction based on SCBO method

In the development of an efficient inversion framework for FMT, we treat the entire objective function $E(X)$ as an expensive-to-evaluate black-box function, $f(X) = E(X)$. Our goal is to find the global minimum $X^* = \underset{X}{\mathrm{argmin}} E(X)$. Given the high dimensionality and the computational cost of evaluating $f(X)$, we employ a surrogate-driven adaptive global optimization strategy, namely the SCBO method.

The SCBO method consists of two primary stages:

(1) *Surrogate Model Construction:* A probabilistic model is built to approximate the complex mapping from a candidate solution X to its objective function score $f(X)$.

(2) *Acquisition Function Optimization:* An acquisition function guides the search process by identifying the most promising points to evaluate next, efficiently balancing exploration, which involves sampling in areas with high uncertainty, and exploitation, which focuses on sampling near the current best solution.

2.2.1. Surrogate model construction based on SPGP

To manage the high-dimensional optimization and alleviate the computational burden, we employ a sparse pseudo-input Gaussian process (SPGP) [44] as a surrogate model for the objective function $f(X)$. Unlike classical Gaussian process regression (GPR) [45], which scales poorly with the number of training points N and typically incurs $O(N^3)$ computational complexity, the SPGP achieves significant efficiency gains by introducing a set of M pseudo-input vectors $Z = \{Z_1, Z_2, \bullet\bullet\bullet, Z_M\}$, where $M \ll N$. These pseudo-inputs serve as latent inducing variables drawn from the Gaussian process prior, effectively defining a low-dimensional subspace that sparsely approximates the full covariance structure. Collectively, they act as approximate support points for the function, enabling a sparse representation of the original covariance matrix. Without loss of generality, the inducing variables $u = f(Z)$ are assumed to follow the following joint Gaussian distribution:

$$u = f(Z)\ \mathcal{N}(0, K_{Z,Z}) \tag{6}$$

where $K_{Z,Z}$ is the covariance matrix among the pseudo-input set.

The objective is to predict the value of the objective function at an arbitrary new input X_*, denoted as $f(X^*) = E(X)$, based on the available training data $\mathscr{D} = \{X_i, f_i\}_{i=1}^N$. It should be emphasized that f_i corresponds to the observed residuals generated by the black-box forward model at the i-th input sample X_i. When the effect of measurement noise is taken into account, the observed values f_i are considered to be corrupted by Gaussian noise relative to the true function values.

Based on the derivation in reference [44], following the introduction of pseudo-input variables, the true function values and the observed data are assumed to be conditionally independent given the inducing variables. Under this assumption, the model is formulated as the following joint distribution:

$$p(f, f^*|u) = p(f|u) \bullet p(f^*|u) \tag{7}$$

By regarding the inducing variables as surrogate points for the training samples, the original covariance matrix is approximated through the covariance between the training data and the inducing points. Based on the sparse approximation framework, the posterior distribution of the training data f is formulated as:

$$p(f|u) = \mathcal{N}(K_{XZ}K_{ZZ}^{-1}u, \Lambda) \tag{8}$$

where $\Lambda := diag(K_{XX} - Q_{XX}) + \sigma^2 I$ and $Q_{XX} := K_{XZ}K_{ZZ}^{-1}K_{ZX}$, with K_{XZ} being the covariance matrix between the training points and the pseudo-inputs, and σ^2 being the variance of the observation noise.

When the pseudo-input points are capable of effectively representing the prior distribution of the function, $K_{XX} \approx Q_{XX}$ is satisfied. Under this condition, by combining Eq. (7) and Eq. (8), the marginal likelihood of the joint posterior distribution can be derived. After integration over the inducing variables u, it is expressed as:

$$p(f) = \int p(f|u)p(u)du \approx \mathcal{N}(0, Q_{XX} + \Lambda) \tag{9}$$

The hyperparameters of the kernel function and the positions of the pseudo-input points are determined by maximizing the marginal likelihood. Upon completion of the training, predictions can be generated for any new input X^*. The posterior distribution is a conditional Gaussian distribution, obtained through Bayes' theorem:

$$p(f^*|f) = \int p(f^*|u)p(u|f)du \tag{10}$$

For the purpose of derivation, the following auxiliary variables are defined:

$$\begin{cases} \mu(X^*) = K_{*Z}(K_{ZZ} + K_{ZX}\Lambda^{-1}K_{XZ})^{-1}K_{ZX}\Lambda^{-1}f \\ \Sigma(X^*) = K_{**} - K_{*Z}(K_{ZZ} + K_{ZX}\Lambda^{-1}K_{XZ})^{-1}K_{Z*} \end{cases} \tag{11}$$

The predictive outcomes of the surrogate model are subsequently presented as follows:

$$f(X^*)\ \mathcal{N}(\mu(X^*), \Sigma(X^*)) \tag{12}$$

where $\mu(X^*)$ is the predicted mean and $\Sigma(X^*)$ is the predicted variance. This SPGP model provides an efficient way to predict both the expected value and the uncertainty of the objective function at any candidate point X^*.

2.2.2. Acquisition function computation based on CLSF

With the SPGP surrogate model, we must now decide which point X^* to evaluate next. This is guided by an acquisition function $L(X^*)$. We employ a reparameterized Monte Carlo (MC) approximation [46] to define a multi-point acquisition function, which allows for efficient gradient propagation and optimization.

The Constrained Least Squares Fitting (CLSF) method [47] is

introduced to accurately compute the acquisition function. This method serves as an effective technique for optimizing the objective function under constraints. Specifically, CLSF simultaneously models both the objective function and the constraints, learns the decision boundary, and minimizes the error between them. In this manner, an efficient search for the global optimal solution is facilitated. CLSF is employed as the acquisition function to guide the sampling process.

For a standard Gaussian process model, the predictive distribution of the objective function is expressed as follows:

$$f(X^*)\ \mathcal{N}(\mu(X^*), \Sigma(X^*)) \tag{13}$$

The distribution is consistent with the predicted result presented in Equation (13). To incorporate the constraints and facilitate effective optimization, a reparameterization technique is employed. This technique transforms the random variable $f(X^*)$ into a standard normal variable $z \sim \mathcal{N}(0,1)$, and the objective function is optimized through appropriate weighting adjustments.

Within this framework, the acquisition function $L(X^*)$ is defined as the expected prediction of the objective function $f(X^*)$ at the current design point X^*, as illustrated below:

$$L(X^*) = \mathbb{E}_{f\ \mathrm{N}(\mu(\mathrm{X}),\Sigma(\mathrm{X}))}[f(X^*)] \tag{14}$$

To evaluate the aforementioned expectation, the MC approach is utilized to generate samples from the Gaussian distribution. The predictive estimate is subsequently approximated with L samples, leading to the following formulation:

$$L(X^*) \approx \frac{1}{L}\sum_{l=1}^{L} f^{(l)}(X^*) \tag{15}$$

where $f^{(l)}(X^*)\ \mathcal{N}(\mu(X^*), \Sigma(X^*))$, $\mu(X^*)$ is the predictive mean and $\Sigma(X^*)$ is the predictive covariance of the Gaussian process at the point X^*, representing the function value obtained from the l-th sample of the posterior distribution.

Building upon the CLSF method, the definition of the acquisition function is further extended to address constrained optimization problems. Within the CLSF framework, the acquisition function is expressed as follows:

$$L_{CLSF}(X^*) = \int_{-\infty}^{\infty} \frac{\pi}{2}|\sigma(X^*)z|\mathcal{N}(z;0,1)dz \tag{16}$$

Here,

$$\sigma(X^*) = \frac{\pi}{2}\int_{-\infty}^{\infty}|\sigma z|\mathcal{N}(z;0,1)dz = \frac{\pi}{2}\mathbb{E}|\sigma Z| \tag{17}$$

By applying the variable transformation $\delta \equiv f(X^*) - \mu(X^*)\ \mathcal{N}(0, \sigma^2(X^*))$, Eq. (14) is equivalently expressed in the following form:

$$L_{CLSF}(X^*) = \frac{\pi}{2}\int_{-\infty}^{\infty}|\delta|\mathcal{N}(\delta;0,\sigma^2(X^*))d\delta \tag{18}$$

It is assumed that the sparse pseudo-input Gaussian process predicts $f(X^*)\ \mathcal{N}(\mu(X^*), \Sigma(X^*))$ with sufficient precision. Consequently, the estimates of $\mu(X^*)$ and $\sigma(X^*)$ are regarded as reliable. Let $\delta \equiv f(X^*) - \mu(X^*)$. Based on this definition, the MC approximation of the acquisition function is given by:

$$L_{CLSF}(X^*) \approx \frac{1}{N_s}\sum_{i=1}^{N_s}\frac{\pi}{2}|f^{(i)}(X^*) - \mu(X^*)| \tag{19}$$

where N_s is the number of samples.

Since the acquisition function CLSF must be maximized, the MC approximation of the multi-point acquisition function is derived from the predictions provided by the SPGP, as described below:

$$L_{CLSF}\left(X_1^*, \cdots, X_q^*\right) \approx \frac{1}{N_s}\sum_{i=1}^{N_s}\underset{j=1,\cdots,q}{max}\{\frac{\pi}{2}|f^{(i)}(X_j^*) - \mu(X_j^*)|\} \tag{20}$$

Where $N_s$is the number of MC samples, $f^{(i)}(X_j^*)\ N(\mu(X_j^*), \Sigma(X_j^*))$ is the i-th sampled value of the objective function evaluated at X_j^*, $\mu(X_j^*)(1 \le j \le q)$ is the predicted value of the objective function at X_j.

The procedure is then iteratively executed until the objective function attains an optimal value, at which stage the iteration is concluded. The computational workflow of the SCBO method is outlined in Algorithm 1.

Algorithm 1. *SCBO Algorithm.*

Input: *System matrix A, measured surface data Φ, initial dataset $\mathscr{D}$, number of MC samples N_s, acquisition function $L(\cdot)$, maximum number of iterations N.*
While $i < N$
Select q new candidate points $\{X_1^*, \cdots, X_q^*\}$ by maximizing the multi-point acquisition function $L(\bullet)$ based on the current surrogate model.
Evaluate the true objective function $f\left(X_j^*\right) = E(X_j^*)$ for each candidate point $j = 1, \ldots, q$.
Augment the dataset: $\mathscr{D} \leftarrow \mathscr{D} \cup \{(X_j^*, f(X_j^*))\}_{j=1}^{q}$.
Update the SPGP surrogate model using the new dataset $\mathscr{D}$.
End While
Output: *Optimal fluorescence yield distribution X^*.*

3. Experiment design

To validate the performance of the proposed SCBO method, we designed a comprehensive set of numerical simulations and an implantation experiment. We evaluated its performance in terms of localization accuracy, morphological fidelity, spatial resolution, and robustness to noise. Furthermore, the outcomes were compared with those obtained using the Graph-TV [16], RLS-DLA [20], and SBL-LCGL [31] methods. All algorithms were implemented in MATLAB and Python and executed on a personal computer equipped with an Intel(R) Core (TM) i5-10210U CPU (1.60 GHz) and 8 GB of RAM.

3.1. Evaluation metrics

The experiment employed position error (PE) [48], Dice coefficient (DICE) [49], normalized mean square error (NMSE) [50], and volume ratio (VR) [31] as quantitative evaluation metrics. The computation efficiency (Time) under this device was also recorded to precisely assess the performance of the SCBO method.

PE is determined by computing the Euclidean distance between the center (X_r, Y, Z_r) and the true center (X_t, Y_t, Z_t). It is employed to assess the accuracy of spatial localization. The PE value ranges from 0 to positive infinity, with lower values denoting greater localization precision.

$$PE = \sqrt{(X_r - X_t)^2 + (Y_r - Y_t)^2 + (Z_r - Z_t)^2} \tag{21}$$

DICE is employed to quantify the overlap between the true target region R_t and the reconstructed target region R_r. Its value ranges from 0 to 1, with larger values indicating a higher degree of similarity between the two regions.

$$DICE = 2\frac{|R_t \cap R_r|}{|R_t| + |R_r|} \tag{22}$$

NMSE is utilized to quantify the relative discrepancy between the true source location N_t and the reconstructed source location N_r. Its value ranges from 0 to positive infinity, with lower values indicating that the reconstructed location closely approximates the true source, thereby reflecting enhanced reconstruction accuracy.

$$NMSE = \frac{\|N_r - N_t\|_2^2}{\|N_t\|_2^2} \tag{23}$$

VR is utilized to quantify the degree of correspondence in both shape and volume between the true light source tetrahedron V_t and the reconstructed light source tetrahedron V_r. VR values approaching 1 signify that the reconstructed source volume closely approximates that of the true source.

$$VR = \frac{V_t}{V_r} \tag{24}$$

3.2. Numerical simulation experiments

In the numerical simulation experiments, a cylindrical model was employed to represent biological tissues. As shown in Fig. 1(a), the model comprised five organs: muscle, heart, lung, bone, and liver. Spherical sources of varying diameters and locations were utilized to simulate fluorescent emitters. The optical parameters of each organ are summarized in Table 1 [51]. The experimental procedure was conducted in two stages: forward simulation and inverse reconstruction. During the forward simulation, photon propagation was computed using tetrahedral elements, and the fluorescence distribution on the model surface was simulated with the molecular optical simulation environment (MOSE, version 2.3) [52], which is based on the Monte Carlo method, as illustrated in Fig. 1(c). In the inverse reconstruction stage, the geometric model was discretized into a uniform tetrahedral mesh using the COMSOL Multiphysics 6.1 platform (COMSOL, Inc., Burlington, Massachusetts, USA), as presented in Fig. 1(b). Based on the generated mesh and the forward simulation results, three-dimensional tumor reconstruction was performed in MATLAB R2023a (MathWorks, Inc., Natick, Massachusetts, USA), enabling precise localization of all luminescent sources within the biological tissues and acquisition of their spatial distribution information.

To assess the performance of the SCBO method, three numerical simulation experiments were conducted, including single-source simulation, dual-source simulation, and anti-noise experiments. In the single-source experiment, a spherical fluorescence source with a radius of 1 mm was positioned at coordinates (−4, 5, 5) mm. In the dual-source experiment, two spherical sources with identical radii of 1 mm were placed at (−1, 3, 7) mm and (−1, 3, 11) mm. For the anti-noise experiment, Gaussian noise at levels of 5 %, 10 %, 15 %, 20 %, and 25 % was added to the single-source measurement data. These experiments enabled a comprehensive assessment of the SCBO method, demonstrating its superiority in reconstruction accuracy and robustness under varying noise conditions.

3.3. Implantation experiment

With the approval of the Animal Ethics Committee of Northwest University of China, an implantation experiment was conducted to further assess the performance of the SCBO method. Eight-week-old BALB/c nude mice were selected, and spherical fluorescent beads containing Cy5.5 solution with a radius of 1 mm were implanted *in vivo*. The true center coordinates of the fluorescent targets were (12.5, 13, 19.5) mm. To minimize animal discomfort, all procedures were performed under isoflurane gas anesthesia. Experimental data were acquired using a dual-modality FMT/CT imaging system, as illustrated in Fig. 2. In this system, FMT was employed to obtain optical information, while CT was utilized to provide anatomical details. Therefore, the imaging workflow can be divided into two stages: optical data acquisition and subsequent data processing.

During the data acquisition stage, a spherical fluorescent bead was implanted into the mouse as a fluorescence target. The bead was subsequently excited six hours later using a 680 nm continuous-wave optical laser (BS750-6WGA, China). The resulting emission was filtered by an optical bandpass filter (FB820-10, THORLABS, USA) and immediately captured by an electron-multiplying CCD (EMCCD) camera (PIX-IS2048B, Princeton Instruments, USA) operated at −80 °C (iXonEM + 888). After fluorescence acquisition, computed tomography (CT) imaging was performed using a flat-panel detector (C7921CA-02, Hamamatsu, Japan) coupled with an X-ray source (5000 Series, Oxford Instruments, CA) to obtain anatomical information. The rotational stage (MRS201, Beijing Optics Instruments Factory, China) and translational stage (MTS314, Beijing Optics Instruments Factory, China) were employed as system control modules, guaranteeing precise operation of each step throughout the imaging procedure.

During the data processing stage, the CT images were processed into three-dimensional volume data, and Amira 2019.1 software (Amira, Visage Imaging, Australia) was used to segment the major organs, including muscle, heart, lung, stomach, liver, and kidney, which were then integrated into the mouse trunk model. The head and tail of the mouse were removed, preserving only the main body region, as shown in

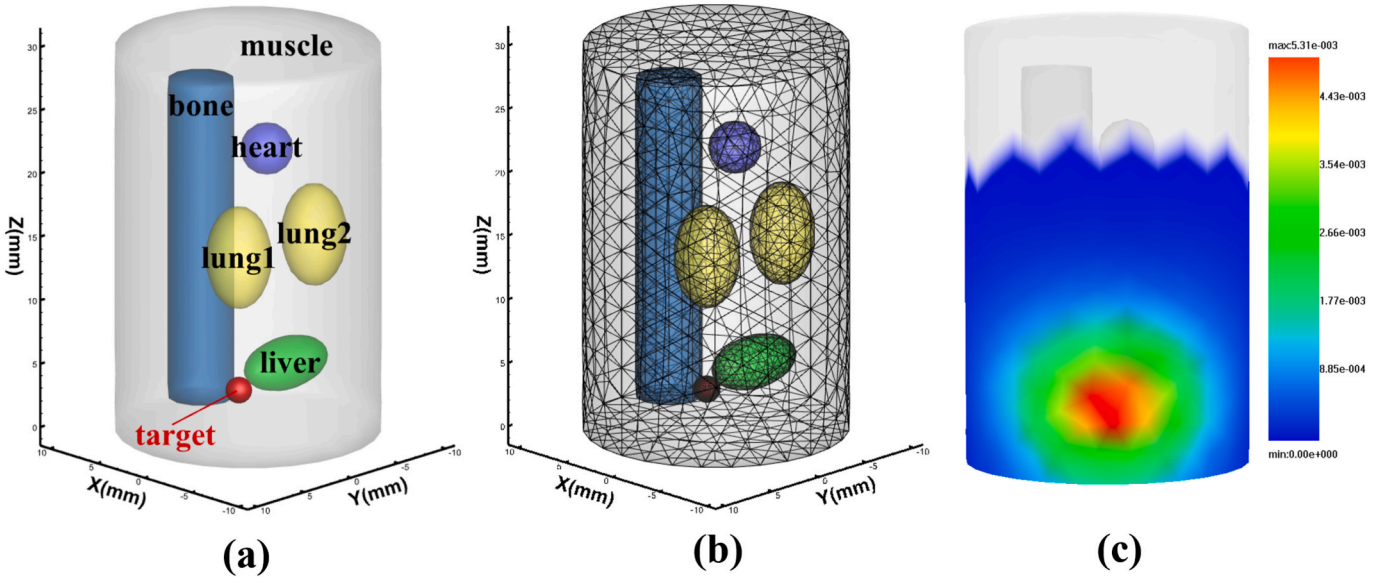

Fig. 1. The numerical simulation setup. (a) The heterogeneous cylindrical phantom, showing the location of internal organs and the fluorescent target. (b) The tetrahedral mesh generated for the inverse reconstruction. (c) The simulated surface fluorescence distribution generated by the Monte Carlo forward model.

Table 1
Optical parameters of the heterogeneous cylindrical phantom.

Tissues	$\mu_{ax}(mm^{-1})$	$\mu_{sx}'(mm^{-1})$	$\mu_{am}(mm^{-1})$	$\mu_{sm}'(mm^{-1})$	g	n
muscle	0.075	0.412	0.047	0.312	0.97	1.37
heart	0.050	0.944	0.033	0.820	0.90	1.37
bone	0.168	2.157	0.105	2.048	0.93	1.55
lung	0.052	2.442	0.033	2.114	0.93	1.03
liver	0.302	0.668	0.192	0.602	0.93	1.38

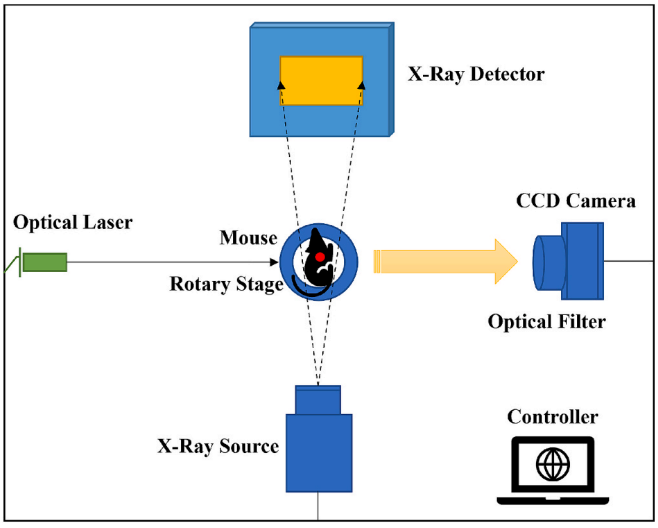

Fig. 2. The chief components of the dual-modality FMT/CT system.

Fig. 3(a). The two-dimensional fluorescence images acquired by the FMT system were subsequently projected onto the three-dimensional surface of the mouse using registration points, as illustrated in Fig. 3 (b) and Fig. 3(c).

4. Results

4.1. Numerical simulation experiments

4.1.1. Single-source simulation experiment

The results of the single-source simulation experiment are presented in Fig. 4 and Table 2. Qualitatively, the SCBO method produced a reconstruction that most closely matched the true source morphology. In contrast, Graph-TV generated significant diffuse smoothing artifacts, while RLS-DLA and SBL-LCGL both produced overly-convergent boundaries that underestimated the source's true size. In Table 2, it can be observed that the PE of the SCBO method was the lowest, measuring 0.319 mm, which represents a 40.63 % reduction compared with the SBL-LCGL method. In addition, the DICE reached 0.827, which was at least 1.1 times greater than those of the other three methods. Regarding reconstruction accuracy, the NMSE of the SCBO method was 0.0341 mm, at least 34.96 % lower than that of the alternatives. Meanwhile, the highest VR value was achieved, and the computational speed was relatively fast. These results indicate that the fluorescence yield of the reconstructed source obtained by SCBO is closer to the true value, confirming its accuracy and superiority in FMT reconstruction.

4.1.2. Dual-source simulation experiment

The results of the dual-source simulation experiment are shown in Fig. 4 and Table 3. As seen in Fig. 4, SCBO again demonstrated excellent morphological recovery and successfully resolved both sources as distinct objects. In the quantitative analysis listed in Table 3, the PE of the SCBO method was measured as 0.476 mm and 0.517 mm, representing reductions of 36.17 % and 16.87 % compared with the second-best method, SBL-LCGL. Regarding shape reconstruction, the average DICE was 0.803, indicating a high degree of overlap and effective restoration of the actual sources. Moreover, the average NMSE was 0.0185, reflecting superior reconstruction quality, while the VR remained stable around 1, demonstrating high volumetric consistency. The computational efficiency was above average, with no notable increase in processing time. These results indicate that, even under multiple-source conditions, the SCBO method can accurately localize the sources and reliably reconstruct their morphologies, confirming its efficiency, accuracy, and robustness in FMT reconstruction.

4.1.3. Anti-noise experiment

The influence of different levels of Gaussian noise on the reconstruction results of the SCBO method is shown in Fig. 5. Due to the presence of noise, the reconstruction results differ from those obtained

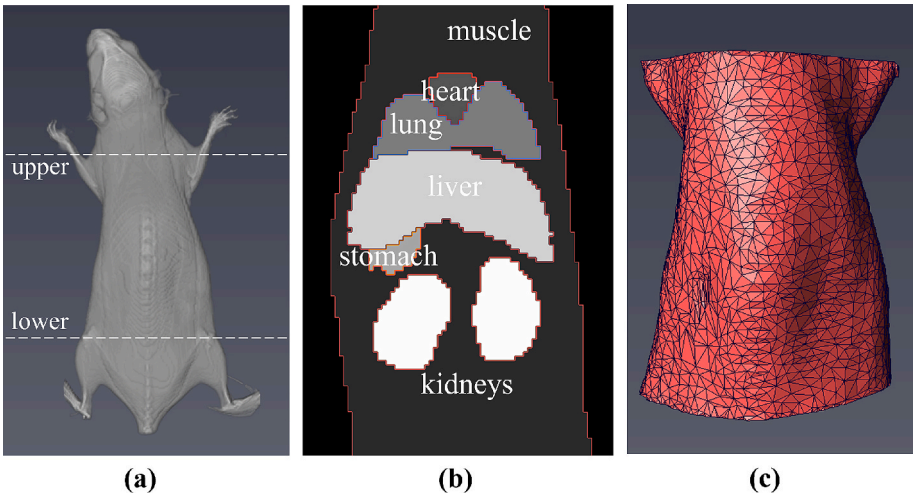

Fig. 3. (a) Intact *in vivo* mouse (cropped along the dashed line). (b) Organ distribution after dissection. (c) Uniform tetrahedral mesh.

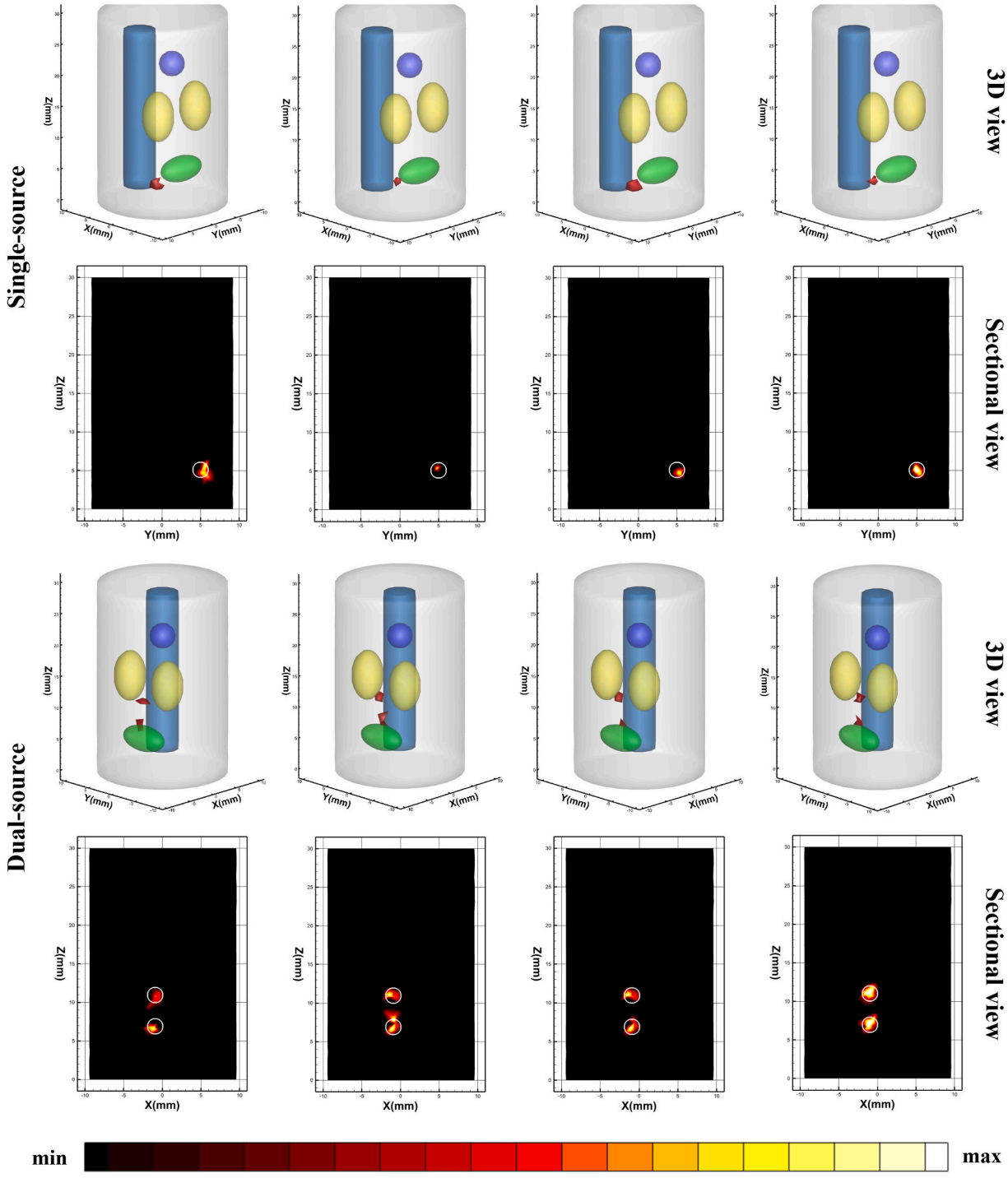

Fig. 4. The first and second rows display the 3D reconstruction results of the four methods under a single-source scenario and the sectional views at $X = -4mm$. The third and fourth rows show the 3D reconstruction results and the sectional views at $Y = 3mm$ under the dual-source scenario. The white circles indicate the true positions of the fluorescent sources, while the red-yellow regions represent the reconstructed locations of the fluorescent sources.

Table 2
Quantitative analysis results of the single-source simulation experiment.

Method	Target source (mm)	Reconstructed source (mm)	PE (mm)	DICE	NMSE	VR	Time (s)
Graph-TV	(−4, 5, 5)	(−4.235, 5.471, 4.695)	1.210	0.267	0.1287	0.330	53.993
RLS-DLA	(−4, 5, 5)	(−4.094, 4.768, 5.351)	0.731	0.753	0.0763	0.358	42.915
SBL-LCGL	(−4, 5, 5)	(−4.201, 5.221, 4.681)	0.537	0.679	0.0524	0.910	41.504
SCBO	(−4, 5, 5)	(−3.915, 4.870, 5.141)	0.319	0.827	0.0341	1.000	39.382

Table 3
Quantitative analysis results of the dual-source simulation experiment.

Method	Target source (mm)	Reconstructed source (mm)	PE (mm)	DICE	NMSE	VR	Time (s)
Graph-TV	(−1, 3, 7)	(−1.541, 3.499, 6.637)	1.898	0.289	0.1139	0.342	57.204
	(−1, 3, 11)	(−1.430, 3.727, 11.099)	1.791	0.182	0.1369	0.932	
RLS-DLA	(−1, 3, 7)	(−1.347, 3.211, 6.738)	1.692	0.667	0.0819	0.475	50.169
	(−1, 3, 11)	(−1.471, 3.448, 11.048)	1.318	0.572	0.0755	1.093	
SBL-LCGL	(−1, 3, 7)	(−1.308, 2.926, 6.677)	0.745	0.712	0.0407	0.781	56.185
	(−1, 3, 11)	(−1.368, 3.280, 11.277)	0.622	0.694	0.0547	1.614	
SCBO	(−1, 3, 7)	(−1.206, 2.779, 7.054)	0.476	0.795	0.0161	1.048	52.638
	(−1, 3, 11)	(−1.251, 2.938, 10.859)	0.517	0.811	0.0208	1.147	

in single-source numerical simulations without noise. Gaussian noise levels of 5 %, 10 %, 15 %, 20 %, and 25 % were applied to investigate the variations in PE, DICE, NMSE, and VR. As illustrated in Fig. 5, the SCBO method demonstrated excellent robustness across all noise levels. Specifically, the PE was 0.319 mm in the noise-free condition and increased only to 0.382 mm under 25 % noise, remaining within an acceptable range. The DICE coefficient decreased from 0.827 to 0.749, corresponding to a reduction of merely 9.43 %. The NMSE rose from 0.0341 to 0.0494, indicating moderate variation. The VR remained approximately 1.0 throughout. These results indicate that the SCBO method can effectively suppress the influence of noise, maintaining stable reconstruction performance and demonstrating superior robustness.

4.2. Implantation experiment

The results of the implantation experiment are shown in Fig. 6, with quantitative metrics summarized in Table 4. In Fig. 6, overly convergent source boundaries were produced by the Graph-TV, RLS-DLA, and SBL-LCGL methods. In contrast, the SCBO method achieved superior reconstruction accuracy and more rapid source recovery. As presented in Table 4, the PE of the SCBO method was 0.436 mm, representing a reduction of at least 41.3 % compared with the other approaches. Regarding morphological reconstruction, the DICE reached 0.883, indicating a high degree of spatial overlap. The NMSE was 0.00242 mm, which is 20.9 % lower than that of the second-best method, SBL-LCGL. The volume recovery rate remained ideal at 1.000, and the reconstruction speed was relatively fast. These results further demonstrate the superiority of the SCBO method in FMT reconstruction, highlighting its potential applicability in practical biomedical studies.

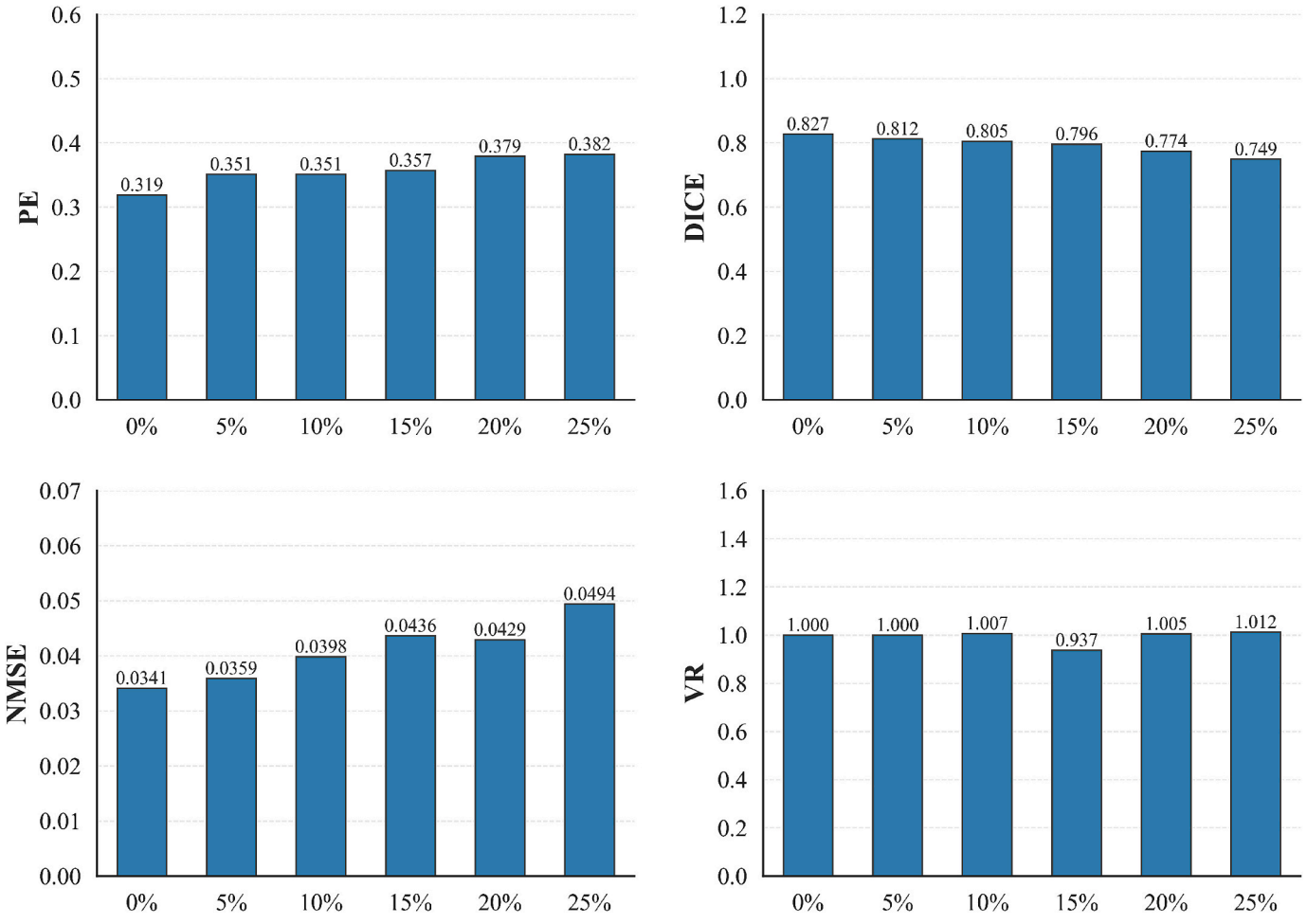

Fig. 5. The quantitative analysis of four methods under different Gaussian noise levels.

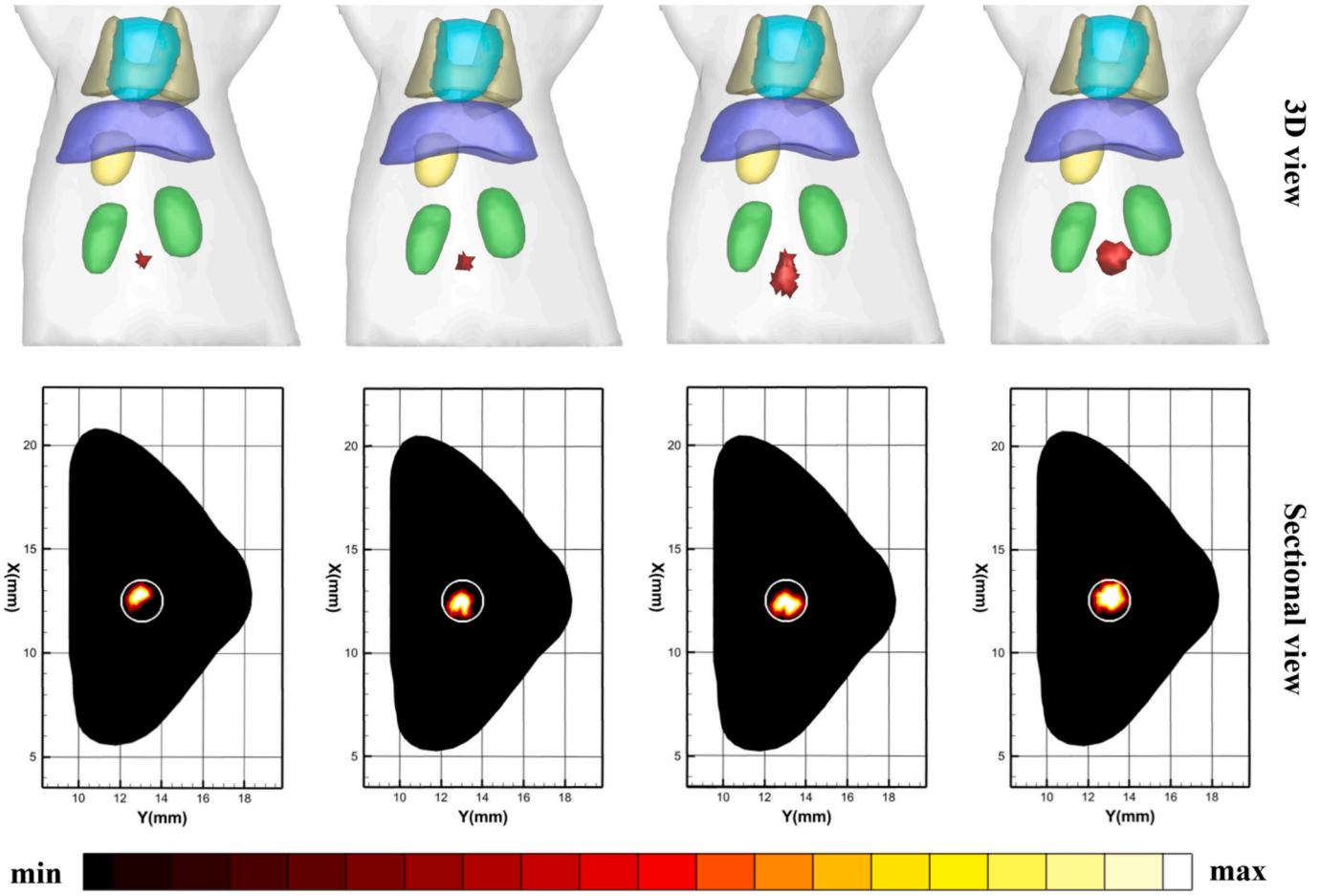

Fig. 6. The first and second rows show the 3D reconstruction results of the four methods for a single source in a mouse and the sectional views at $Z = 19.5mm$. The white circles indicate the true positions of the fluorescent sources, while the red-yellow regions represent the reconstructed locations of the fluorescent sources.

Table 4
Quantitative analysis results of the implantation experiment.

Method	Target source (mm)	Reconstructed source (mm)	PE (mm)	DICE	NMSE	VR	Time (s)
Graph-TV	(12.5,13,19.5)	(12.469,12.932,19.535)	1.651	0.296	0.00942	0.857	473.473
RLS-DLA	(12.5,13,19.5)	(12.453,13.153,19.342)	1.389	0.581	0.00574	1.312	288.486
SBL-LCGL	(12.5,13,19.5)	(12.356,13.125,18.309)	0.743	0.735	0.00306	1.046	334.976
SCBO	(12.5,13,19.5)	(12.495,13.073,19.527)	0.436	0.883	0.00242	1.000	234.772

5. Discussion and conclusion

In this work, a Bayesian optimization approach based on sparse pseudo-input Gaussian processes and constrained least squares fitting (SCBO) was proposed to improve the accuracy of 3D reconstruction of fluorescent sources. The method is centered on constructing a sparse Gaussian process surrogate model using a limited number of inducing points. The covariance among these points is utilized to approximate the full data covariance structure, thereby reducing the computational complexity of training and inference from traditional cubic and quadratic scales to linear and constant levels, while preserving prediction accuracy. To further balance the sparsity of the source distribution with the preservation of geometric integrity, EN regularization was incorporated. EN regularization, which integrates the characteristics of the traditional L_1 and L_2 norms, provides a trade-off between sparsity and smoothness in the reconstructed results. An acquisition function was subsequently designed using the MC method, and a CLFS strategy was applied for sampling point selection. This framework allows for efficient search and rapid convergence, thereby accelerating the optimization and reconstruction process in FMT.

The effectiveness of the SCBO method was verified through three numerical simulation experiments and one implantation experiment. The simulation results and quantitative analyses demonstrated that the SCBO method outperformed the Graph-TV, RLS-DLA, and SBL-LCGL approaches in terms of localization precision, morphological reconstruction, and dual-source discrimination. Superior performance was observed across four evaluation indices, including PE, DICE, NMSE, and VR, highlighting significant enhancements in source positioning and structural recovery. The anti-noise experiment further indicated that the SCBO method maintained high robustness despite the progressive increase in noise intensity. In addition, the implantation experiment confirmed the practicality of this approach for detecting radioactive sources in living organisms, thereby providing strong evidence for its applicability in preclinical research and potential clinical implementation.

Although the SCBO method has achieved satisfactory performance,

several limitations still exist in practical applications. Firstly, because a staged solving strategy is adopted, the overall computational cost remains relatively high when processing large-scale datasets. Secondly, the quantitative assessment of the interference caused by low fluorescence signals in non-target regions on fluorescence distribution acquisition has not yet been performed. In addition, the adaptability of the method to various tissue optical properties has not been comprehensively evaluated. Future studies will be devoted to optimizing the computational framework and integrating automated inducing-point selection to further reduce computational complexity and enhance algorithmic robustness. Furthermore, systematic *in vivo* experiments will be conducted in more complex biological environments to verify the stability of the method under diverse optical conditions. Finally, the potential of SCBO will be further explored in multimodal imaging, such as PET/CT fusion, in larger animal models, and on real patient datasets, thereby facilitating its translation from preclinical studies to clinical applications.

In summary, the SCBO method was developed to address the inverse problem of FMT by generating a limited number of inducing points to approximate the covariance structure of the original data. EN regularization was introduced to achieve a balanced trade-off between source sparsity and morphological fidelity. Moreover, a MC sampling strategy was employed to construct the acquisition function, while a CLSF was adopted to optimize the sampling procedure, enabling efficient selection of sampling points. The proposed SCBO framework effectively mitigated the influence of errors on reconstruction accuracy, alleviated oversparsity, and improved morphological recovery. Numerical simulations and implantation experiments were carried out to compare SCBO with Graph-TV, RLS-DLA, and SBL-LCGL methods. The reconstruction results revealed that SCBO achieved superior localization precision and morphological restoration in tumor regions, showing lower PE and NMSE, higher DICE, and better VR and reconstruction efficiency, thereby demonstrating its robustness and reliability. Overall, this study provides a promising approach for improving FMT reconstruction accuracy and has potential for further application in preclinical and clinical biomedicine.

CRediT authorship contribution statement

Xin Cao: Supervision, Resources, Investigation. **Yiting He:** Writing – original draft, Methodology. **Xin Zhou:** Formal analysis. **Jiaxin Du:** Validation. **Yi Chen:** Formal analysis. **Chengyi Gao:** Validation. **Huangjian Yi:** Formal analysis. **Xingxing Hao:** Writing – review & editing. **Linzhi Su:** Funding acquisition.

Declaration of competing interest

The authors declare that they have no known competing financial interests or personal relationships that could have appeared to influence the work reported in this paper.

Acknowledgments

This work was supported in part by the National Major Scientific Research Instrument Development Projects of China (82127805), in part by the Key Research and Development Program of Shaanxi Province (2024SF-YBXM-681).

Data availability

Data underlying the results presented in this paper are not publicly available at this time but may be obtained from the authors upon request.

References

[1] V. Ntziachristos, Fluorescence molecular imaging, Annu. Rev. Biomed. Eng. 8 (1) (2006) 1–33.
[2] M. Koch, P. Symvoulidis, V. Ntziachristos, Tackling standardization in fluorescence molecular imaging, Nat. Photonics 12 (9) (2018) 505–515.
[3] B. Zhu, J.C. Rasmussen, E.M. Sevick-Muraca, A matter of collection and detection for intraoperative and noninvasive near-infrared fluorescence molecular imaging: to see or not to see? Med. Phys. 41 (2) (2014) 022105.
[4] R. Weissleder, M. Nahrendorf, Advancing biomedical imaging, Proc. Natl. Acad. Sci. 112 (47) (2015) 14424–14428.
[5] Z. Hu, M. Zhao, Y. Qu, X. Zhang, M. Zhang, M. Liu, H. Guo, Z. Zhang, J. Wang, W. Yang, In vivo 3-dimensional radiopharmaceutical-excited fluorescence tomography, J. Nucl. Med. 58 (1) (2017) 169–174.
[6] X. Ding, K. Wang, B. Jie, Y. Luo, Z. Hu, J. Tian, Probability method for Cerenkov luminescence tomography based on conformance error minimization, Biomed. Opt. Express 5 (7) (2014) 2091–2112.
[7] D. Zhu, C. Li, Nonconvex regularizations in fluorescence molecular tomography for sparsity enhancement, Phys. Med. Biol. 59 (12) (2014) 2901–2912.
[8] A. Daducci, D. Van De Ville, J.-P. Thiran, Y. Wiaux, Sparse regularization for fiber ODF reconstruction: from the suboptimality of $\ell 2$ and $\ell 1$ priors to $\ell 0$, Med. Image Anal. 18 (6) (2014) 820–833.
[9] Q. Zhang, H. Zhao, D. Chen, X. Qu, X. Chen, X. He, W. Li, Z. Hu, J. Liu, J. Liang, Source sparsity based primal-dual interior-point method for three-dimensional bioluminescence tomography, Opt. Commun. 284 (24) (2011) 5871–5876.
[10] H. Guo, Z. Hu, X. He, X. Zhang, M. Liu, Z. Zhang, X. Shi, S. Zheng, J. Tian, Non-convex sparse regularization approach framework for high multiple-source resolution in Cerenkov luminescence tomography, Opt. Express 25 (23) (2017) 28068–28085.
[11] P. Jiao, H. Yi, Y. Hu, X. He, A permissible region strategy for fluorescence molecular tomography, Opt. Rev. 26 (6) (2019) 523–530.
[12] H. Zhang, X. He, J. Yu, X. He, H. Guo, Y. Hou, L1-L2 norm regularization via forward-backward splitting for fluorescence molecular tomography, Biomed. Opt. Express 12 (12) (2021) 7807–7825.
[13] X. He, H. Meng, X. He, K. Wang, X. Song, J. Tian, Nonconvex laplacian manifold joint method for morphological reconstruction of fluorescence molecular tomography, Mol. Imaging Biol. 23 (3) (2021) 394–406.
[14] P.-A. Gauthier, P. Lecomte, A. Berry, Source sparsity control of sound field reproduction using the elastic-net and the lasso minimizers, J. Acoust. Soc. Am. 141 (4) (2017) 2315–2326.
[15] G. Zhang, J. Zhang, Y. Chen, M. Du, K. Li, L. Su, H. Yi, F. Zhao, X. Cao, Logarithmic total variation regularization via preconditioned conjugate gradient method for sparse reconstruction of bioluminescence tomography, Comput. Methods Programs Biomed. 243 (2024) 107863.
[16] W.-Z. Shao, H.-S. Deng, W.-W. Luo, J.-Y. Li, M.-L. Liu, Revisiting reweighted graph total variation blind deconvolution and beyond, Vis. Comput. 40 (5) (2024) 3119–3135.
[17] C. Bao, H. Ji, Y. Quan, Z. Shen, Dictionary learning for sparse coding: Algorithms and convergence analysis, IEEE Trans. Pattern Anal. Mach. Intell. 38 (7) (2015) 1356–1369.
[18] H. Su, F. Xing, L. Yang, Robust cell detection of histopathological brain tumor images using sparse reconstruction and adaptive dictionary selection, IEEE Trans. Med. Imaging 35 (6) (2016) 1575–1586.
[19] Q. Liu, S. Wang, L. Ying, X. Peng, Y. Zhu, D. Liang, Adaptive dictionary learning in sparse gradient domain for image recovery, IEEE Trans. Image Process. 22 (12) (2013) 4652–4663.
[20] K. Skretting, K. Engan, Recursive least squares dictionary learning algorithm, IEEE Trans. Signal Process. 58 (4) (2010) 2121–2130.
[21] W. Li, W. Lu, X. Liang, M. Chen, K. Guo, Collaborative Dictionary Learning for Compressed Sensing, IEEE Trans. Ind. Informat. 20 (7) (2024) 9610–9620.
[22] Y. Chun, J.A. Fessler, Convolutional dictionary learning: Acceleration and convergence, IEEE Trans. Image Process. 27 (4) (2017) 1697–1712.
[23] J. Mao, H. He, Deep learning in fluorescence imaging and analysis, J. Intell. Med. 1 (1) (2024) 42–62.
[24] P. Zhang, G. Fan, T. Xing, F. Song, G. Zhang, UHR-DeepFMT: ultra-high spatial resolution reconstruction of fluorescence molecular tomography based on 3-D fusion dual-sampling deep neural network, IEEE Trans. Med. Imaging 40 (11) (2021) 3217–3228.
[25] X. Zhao, L. Zhang, C. Qiu, H. Zhang, X. He, X. Leng, X. He, H. Guo, MSDRN: Multi-scale deep residual network for fluorescence molecular tomography, Comput. Methods Programs Biomed. 276 (2026) 109217.
[26] L. Guo, F. Liu, C. Cai, J. Liu, G. Zhang, 3D deep encoder–decoder network for fluorescence molecular tomography, Opt. Lett. 44 (8) (2019) 1892–1895.
[27] H. Meng, Y. Gao, X. Yang, K. Wang, J. Tian, K-nearest neighbor based locally connected network for fast morphological reconstruction in fluorescence molecular tomography, IEEE Trans. Med. Imaging 39 (10) (2020) 3019–3028.
[28] P. Zhang, C. Ma, F. Song, Z. Liu, H. Wu, Y. Feng, Y. He, D. Wang, G. Zhang, SVRNet: first investigation of single-view reconstruction network for fluorescence molecular tomography, IEEE Trans. Comput. Imaging 9 (2023) 834–845.
[29] H. Zayyani, M. Babaie-Zadeh, C. Jutten, An iterative Bayesian algorithm for sparse component analysis in presence of noise, IEEE Trans. Signal Process. 57 (11) (2009) 4378–4390.
[30] N. Dobigeon, A.O. Hero, J.-Y. Tourneret, Hierarchical Bayesian sparse image reconstruction with application to MRFM, IEEE Trans. Signal Process. 18 (9) (2009) 2059–2070.

[31] X. Li, C.X. Ling, H. Wang, The convergence behavior of naive Bayes on large sparse datasets, ACM Trans. Knowl. Discov. Data 11 (1) (2016) 1–24.
[32] W. Chen, X. Gong, N. Song, Nonconvex robust low-rank tensor reconstruction via an empirical Bayes method, IEEE Trans. Signal Process. 67 (22) (2019) 5785–5797.
[33] Y. Wang, H. Wang, Q. Zhu, Y. Chen, L. Su, H. Yi, C. Gao, X. Cao, SBL-LCGL: sparse Bayesian learning based on Laplace distribution for robust cone-beam x-ray luminescence computed tomography, Phys. Med. Biol. 69 (17) (2024) 175020.
[34] L. Yin, K. Wang, T. Tong, Q. Wang, Y. An, X. Yang, J. Tian, Adaptive grouping block sparse Bayesian learning method for accurate and robust reconstruction in bioluminescence tomography, I.E.E.E. Trans. Biomed. Eng. 68 (11) (2021) 3388–3398.
[35] K. Ray, B. Szabó, Variational Bayes for high-dimensional linear regression with sparse priors, J. Am. Stat. Assoc. 117 (539) (2022) 1270–1281.
[36] X. Wang, Y. Jin, S. Schmitt, M. Olhofer, Recent advances in Bayesian optimization, ACM Comput. Surv. 55 (13s) (2023) 1–36.
[37] X. Cao, Y. He, X. Zhou, J. Du, Y. Chen, Y. Liu, C. Gao, Adagrad-optimized variational Bayesian reconstruction with sparsity-adaptive normal-generalized inverse Gaussian prior for fluorescence molecular tomography, J. Appl. Phys. 138 (24) (2025).
[38] X. Xiong, J. Huang, S. Li, J. He, S. Wang, Dual-phase multiobjective Bayesian optimization method for estimating hepatocellular carcinoma dynamics parameters from PET/CT scans, Quant. Imaging Med. Surg. 15 (8) (2025) 6654–6666.
[39] B. Yang, Y. He, N. Cai, J. Zhang, Y. Chen, Y. Liu, C. Gao, H. Yi, X. Cao, Adaptive Bayesian augmented Lagrangian algorithm for fluorescence molecular tomography, J. Opt. Soc. Am. A 43 (1) (2025) 204–213.
[40] Z. Valibeiglou, J.P. Islamian, Y. Soleymani, S. Farzanehfar, F. Aghahosseini, N. Gilani, A. Rahmin, P. Sheikhzadeh, Enhancing radiomics robustness using bayesian penalized likelihood PET reconstruction: application to Phantom and non-small cell lung cancer patient studies, BMC Med. Imaging 25 (1) (2025) 223.
[41] Q. Zhang, H. Zhao, D. Chen, X. Qu, X. Chen, X. He, W. Li, Z. Hu, J. Liu, J. Liang, Source sparsity based primal-dual interior-point method for three-dimensional bioluminescence tomography, Opt. Commun. 284 (24) (2011) 5871–5876.
[42] A.D. Klosea, B.J. Beattieb, H. Dehghanic, L. Vider, C. Le, V. Ponomarev, R. Blasberg, In vivo bioluminescence tomography with a blocking-off finite-difference SP 3 method and MRI/CT coregistration, Med. Phys. 37 (1) (2009) 329–338.
[43] H. Li, L. Ding, Generalized conditional gradient method for elastic-net regularization, J. Comput. Appl. Math. 403 (2022) 113872.
[44] E. Snelson, Z. Ghahramani, Sparse Gaussian Processes using Pseudo-inputs, Adv. Neural Inf. Process. Syst. 18 (2005).
[45] C. Huang, Y. Ren, E.K. McGuinness, M.D. Losego, R.P. Lively, V.R. Joseph, Bayesian optimization of functional output in inverse problems, Optim. Eng. 22 (4) (2021) 2553–2574.
[46] J. Wilson, F. Hutter, M. Deisenroth, Maximizing acquisition functions for Bayesian optimization, Adv. Neural Inf. Process. Syst. 31 (2018).
[47] F.S. Costabal, P. Perdikaris, E. Kuhl, D.E. Hurtado, Multi-fidelity classification using Gaussian processes: accelerating the prediction of large-scale computational models, Comput. Methods Appl. Mech. Eng. 357 (2019) 112602.
[48] Y. An, J. Liu, G. Zhang, J. Ye, Y. Du, Y. Mao, C. Chi, J. Tian, A novel region reconstruction method for fluorescence molecular tomography, I.E.E.E. Trans. Biomed. Eng. 62 (7) (2015) 1818–1826.
[49] Y. Chen, W. Li, M. Du, L. Su, H. Yi, F. Zhao, K. Li, L. Wang, X. Cao, Elastic net-based non-negative iterative three-operator splitting strategy for Cerenkov luminescence tomography, Opt. Express 30 (20) (2022) 35282–35299.
[50] Y. Yuan, H. Guo, H. Yi, J. Yu, X. He, X. He, Correntropy-induced metric with Laplacian kernel for robust fluorescence molecular tomography, Biomed. Opt. Express 12 (10) (2021) 5991–6012.
[51] S.L. Jacques, Optical Properties of Biological Tissues: a Review, Phys. Med. Biol. 58 (11) (2013) R37–R61.
[52] N. Ren, J. Liang, X. Qu, J. Li, B. Lu, J. Tian, GPU-based Monte Carlo simulation for light propagation in complex heterogeneous tissues, Opt. Express 18 (7) (2010) 6811–6823.